PAPER • OPEN ACCESS

Growth dynamics and compositional structure in periodic InAsSb nanowire arrays on Si (111) grown by selective area molecular beam epitaxy

View the article online for updates and enhancements.

Growth dynamics and compositional structure in periodic InAsSb nanowire arrays on Si (111) grown by selective area molecular beam epitaxy

Daniel Ruhstorfer[1] , Armin Lang[1], Sonja Matich[1], Markus Döblinger[2], Hubert Riedl[1], Jonathan J Finley[1] and Gregor Koblmüller[1]

[1] Walter Schottky Institute and Physics Department, Technical University of Munich, Garching, Germany
[2] Department of Chemistry, Ludwig-Maximilians-University Munich, Munich, Germany

E-mail: Gregor.Koblmueller@wsi.tum.de

CrossMark

Abstract

We report a comprehensive study of the growth dynamics in highly periodic, composition tunable InAsSb nanowire (NW) arrays using catalyst-free selective area molecular beam epitaxy. Employing periodically patterned SiO_2-masks on Si (111) with various mask opening sizes (20–150 nm) and pitches (0.25–2 μm), high NW yield of $>90\%$ (irrespective of the InAsSb alloy composition) is realized by the creation of an As-terminated 1×1-Si(111) surface prior to NW nucleation. While the NW aspect ratio decreases continually with increasing Sb content (x_{Sb} from 0% to 30%), we find a remarkable dependence of the aspect ratio on the mask opening size yielding up to $\sim$8-fold increase for openings decreasing from 150 to 20 nm. The effects of the interwire separation (pitch) on the NW aspect ratio are strongest for pure InAs NWs and gradually vanish for increasing Sb content, suggesting that growth of InAsSb NW arrays is governed by an In surface diffusion limited regime even for the smallest investigated pitches. Compositional analysis using high-resolution x-ray diffraction reveals a substantial impact of the pitch on the alloy composition in homogeneous InAsSb NW arrays, leading to much larger x_{Sb} as the pitch increases due to decreasing competition for Sb adatoms. Scanning transmission electron microscopy and associated energy-dispersive x-ray spectroscopy performed on the cross-sections of individual NWs reveal an interesting growth-axis dependent core–shell like structure with a discontinuous few-nm thick Sb-deficient coaxial boundary layer and six Sb-deficient corner bands. Further analysis evidences the presence of a nanoscale facet at the truncation of the (111)B growth front and {1-10} sidewall surfaces that is found responsible for the formation of the characteristic core–shell structure.

Keywords: InAsSb nanowires, site-selective growth, structural properties, alloy composition properties, molecular beam epitaxy

(Some figures may appear in colour only in the online journal)

1. Introduction

Antimony (Sb) containing InAs nanowires (NW) with tunable alloy composition have emerged as versatile one-dimensional (1D) semiconductors with attractive properties for a wide range of applications. The InAsSb alloys are known to have

very small electron effective mass, high carrier mobility, large *g*-factors, and significant spin–orbit coupling that is even stronger than in their binary compounds (InAs or InSb) [1, 2]. This makes ternary InAsSb NWs a very promising material in, for instance, hybrid semiconductor–superconductor devices for topological quantum information applications [3]. They are also considered important for nanothermoelectrics, due to the possibility for quantized 1D-subband transport [4, 5] along with the highest estimated thermopower and lowest thermal conductivity amongst all III–V semiconductors [6]. Furthermore, the InAsSb alloy system offers a widely tunable band gap throughout most of the mid-infrared (MIR) spectral range ($\sim$2–8 μm) and even the long-wavelength infrared (LWIR) band ($\sim$8–12 μm). In fact, InAsSb with an Sb molar fraction of $x_{sb} \sim 0.65$ has the narrowest room-temperature band gap of $E_g \sim 100$ meV of all III–V semiconductors which corresponds to a wavelength of 12 μm. These features combined with the enhanced light absorption in NWs [7] and the feasibility to monolithically integrate InAsSb NWs with long carrier lifetime on a CMOS-compatible Si platform [8–10] enables advanced forms of MIR-to-LWIR photodetectors for gas sensing [9–11]. Likewise, MIR light sources with operation at room-temperature have also been realized using InAs/InAsSb based NW heterostructures [12].

The vast amount of potential applications clearly motivates efforts to accurately control growth and obtain correlated understanding of physical properties in the InAsSb NW materials system. So far, significant research was aimed at tuning the alloy composition of InAsSb NWs using different growth methods, including metal organic chemical vapor deposition (MOCVD) [8–11, 13–15], molecular beam epitaxy (MBE) [16–19], as well as chemical beam epitaxy [20]. Most studies recognized that the addition of Sb to InAs NWs favors the formation of a zincblende (ZB) phase [13–17] while leading to increased/reduced NW diameter/length, irrespective of the growth method and growth mode [12–14, 16–20]. Nearly phase-pure ZB type InAsSb NWs are found to yield substantially increased charge carrier mobilities, as opposed to e.g. InAs NWs which commonly exhibit intermixed polytypic wurtzite (WZ)-ZB phases with large stacking defect densities [16, 17]. Characteristic differences in the crystal-phase dependent band gap properties [8, 18], along with significant band bowing for intermediate to large Sb contents were also identified [8]. Several efforts were made to develop an understanding for the observed transitions in crystal phase and the distinct reductions in NW aspect ratio with increasing Sb-content. Whereas the stabilization of the ZB phase in InAsSb NWs has been mainly attributed to the low ionicity of the atomic bonds as well as growth kinetics [16, 21, 22], the increased radial growth upon increased Sb supply suggests the presence of an Sb surfactant effect [19, 23–25]. Hereby, Sb reduces not only the surface diffusion of In adatoms but also enhances nucleation and step-flow growth on the NW sidewall surfaces [20], both effects leading to enhanced lateral growth. The inhibited surface diffusion is also often seen by the undesired formation of parasitic clusters in the vicinity of as-grown InAsSb NWs [16, 19]. To influence the surface

diffusion mediated effects and control NW aspect ratio and alloy composition, efforts were directed mainly at tuning V/III ratio and growth temperature [8, 13, 16, 17, 20, 25].

Site-selective, i.e. position-controlled growth of periodic NW arrays with tuneable geometrical parameters is another powerful means to accurately control surface diffusion and growth dynamics. High-periodicity array growth is particularly advantageous in such multi-component NWs, since any undesired deviations in interwire separation (as typical for growth on unpatterned substrates) may lead to substantial dispersion in NW size and composition as previously found in e.g. InGaAs NWs [26, 27]. So far, there are only few examples of selective area epitaxy (SAE) of InAsSb NW arrays, where the effects of array geometry were explored using growth on prepatterned SiO_2/Si (111) substrates: in [8], Farrell *et al* investigated MOCVD-grown InAsSb NW arrays for moderate NW spacing (pitch) of $\sim$600–900 nm under relatively large SiO_2 mask openings (diameters >100 nm). Excellent high-yield/high-uniformity NW arrays were produced with Sb contents up to $\sim$15%, while increases in mask opening size lead to a transformation from NWs to 'pancake'-like structures [8]. Interestingly, in that report the NW aspect ratio dependency on the Sb supply exhibits an opposite behavior to the majority of studies [12–14, 16–20]. Periodic arrays of very thick ($\sim$0.5 μm wide) InAsSb NWs were also grown by catalyst-free selective-area MBE using a core–shell approach to enable diameter-dependent absorption resonances in the mid-IR tuned by the NW spacing in the array [28]. Hereby, the evolution of NW diameter was explored upon shell growth, leaving the array geometry dependent Sb incorporation dynamics of directly bottom-up grown InAsSb NWs unresolved. Moreover, MBE-grown catalyst-free InAsSb NW arrays reported to date further suffer from poor NW growth yield, where strategies such as the pre-nucleation of an InAs stem [10, 12, 28–30] were found to be necessary to increase yield.

In the following, we provide a comprehensive investigation of the growth kinetics and Sb incorporation dynamics of highly periodic, catalyst-free InAsSb NW arrays grown by MBE in dependence of a wide set of array geometry parameters and growth conditions. The prime goal is to illustrate the interrelated dynamics between mask opening size, interwire separation, Sb supply and corresponding surface diffusion to map out optimized growth regimes for realizing high-aspect ratio InAsSb NWs with enhanced Sb incorporation. Our study also addresses the issues of vertical NW growth yield, with substantial improvements being realized upon modifications of the Si (111) surface reconstruction prior to NW growth. The growth dynamic dependent morphological data is further correlated with extensive structural and compositional analysis using complementary high-resolution x-ray diffraction (HRXRD), high-resolution (HR-) and scanning transmission electron microscopy (STEM) and associated energy-dispersive x-ray spectroscopy (EDXS). These allow us to further map out a specific radial compositional structure that is decomposed into an unintentional core-interlayer-shell heterostructure—a general feature which is characteristic of SAE-type growth from mask openings.
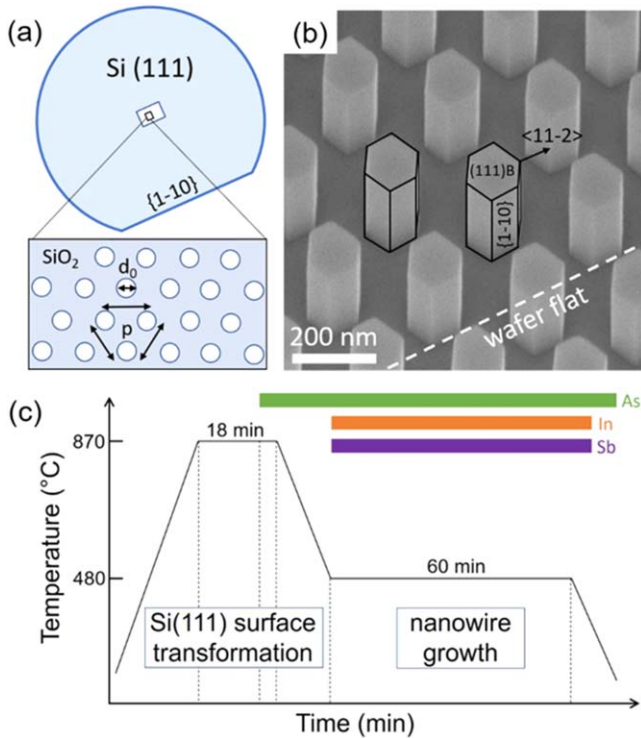
Figure 1. (a) Schematic illustration of the employed Si (111) wafer as growth substrate with its wafer flat parallel to the {1-10} plane. The growth fields patterned into the SiO_2 mask layer in the center of the wafer consist of periodic, hexagonally arranged mask openings with diameter d_0 and pitch p (features are not to scale). (b) SEM image (45° tilted view) of a typical high-yield InAsSb NW array (obtained on array with $d_0 = 130$ nm, pitch $p = 0.25$ μm) from growth series (i) at a $FF_{Sb} = 2\%$. The wafer flat orientation is indicated by the white dashed line. All NWs are well oriented with respect to the wafer flat, indicating that the side facets are {1-10} planes while the edges of the hexagonally shaped NWs point towards the ⟨11-2⟩ directions. (c) Process flow of the employed *in situ* pretreatment and successive growth steps during the MBE growth of catalyst-free InAsSb NWs.

2. Experimental details

All growth experiments were performed in a solid-source Gen-II MBE system equipped with conventional effusion cells for group-III elements (In, Ga, Al) and Veeco valved cracker cells for supply of group-V elements arsenic (As) and antimony (Sb). While the supply of As was provided as uncracked As_4, the corrosive valved cracker cell for Sb was operated under conditions that create cracked Sb_2 molecules. For SAE commercially available single-side polished 2 inch p-type Si (111) wafers were used which feature a 20 nm thick thermally grown SiO_2 mask layer on the surface. Each substrate was prepatterned by electron beam lithography (EBL) and subsequent reactive ion etching to produce periodic mask patterns arranged in hexagonal lattices with nominal circular opening diameters of $d_{0,nom} = 10$–140 nm and pitches of $p = 0.25$–2 μm (see figure 1(a)). The real opening diameters d_0 were also measured by scanning electron microscopy (SEM) and atomic force microscopy and found to be ∼10 nm larger than the nominal values on average. The patterns were altogether arranged in 13 × 5 matrices in the very center of

individual wafers, whereby each field (consisting of 400 holes each) is described by a given combination of mask opening diameter and pitch. On certain substrates we also included larger field sizes of 2 × 2 mm^2 with a fixed opening diameter of $d_0 = 50$ nm and three distinct pitches of 0.25, 0.5 and 1 μm, in order to enable HRXRD measurements for determination of alloy composition. Prior to growth the as-patterned substrates were briefly immersed in buffered oxide etchant (BOE: 98:2 $NH_4F(40\%):HF(50\%)$). This step removes any residual SiO_2 inside the mask openings and guarantees a H-terminated Si (111) surface that inhibits reoxidation during substrate loading and allows SAE of III–V NWs on Si [31].

Producing high-quality selective area growth of InAsSb NWs with very high vertical growth yield and without the use of InAs stems is a major challenge when grown in a catalyst-free vapor–solid (VS) growth mode on Si by MBE We have therefore developed an elaborate *in situ* thermal treatment of the H-terminated Si (111) substrate surface prior to the nucleation and growth of InAsSb NWs, in analogy to our very recent work on SAE of VS-type GaAs NWs [32]. As illustrated in the process flow diagram of figure 1(c), we performed a temperature ramp of the as-loaded substrate to 870 °C and subsequent annealing for ∼15 min that induces H desorption and transforms an intermediate 7 × 7 reconstructed Si (111) surface to a clean 1 × 1 reconstructed surface at the very high temperature [33]. We then supplied a high As-flux as used for the consecutive growth (beam equivalent pressure BEP > 10^{-6} mbar), which stabilizes an As-terminated 1 × 1 Si (111) surface phase while cooling the substrate to the desired growth temperature (e.g. 480 °C). The As-terminated 1 × 1-Si (111) surface ensures proper epitaxial relation of the nucleating [111]B-oriented III–V NWs with the underlying substrate. Finally, growth of catalyst-free InAsSb NWs was induced by simultaneously opening the In and Sb shutters, and growth was performed for 60 min if not otherwise noted. After growth was terminated, the substrate was cooled down to ambient temperatures under excess As. A typical example of an as-grown InAsSb NW array is shown in figure 1(b), illustrating the excellent selectivity and growth yield of close to 100%. All NWs are perfectly aligned with no in-plane misorientation, i.e. the sidewall facets of the NWs are well aligned with respect to the {1-10} wafer flat of the underlying Si (111) substrate wafer, confirming that they are associated with the {1-10} family of planes while the corner facets point towards the ⟨11-2⟩ orientations. In addition, the top facet along the [111]B NW growth orientation is very flat and characteristic of Sb-containing InAs NWs.

Several different growth series were performed: (i) in a first series, we varied the Sb supply under fixed growth time (1 h) and temperature of 480 °C, a constant In flux (0.23 Å s^{-1} as calibrated by reflection high energy electron diffraction [34]), and a fixed As_4 flux (BEP = 3×10^{-6} mbar). Based on calibrated data of equivalent planar growth rates this corresponds to a V/III ratio of ∼7. Note that under these conditions the growth of InAs-based NWs proceeds in a complete catalyst-free manner throughout the entire growth, as confirmed in detailed studies before [34]. The Sb_2 flux was varied depending on the desired fractional flux (FF_{Sb}) relative

to the As-flux ($FF_{Sb} = \Phi_{Sb2}/\Phi_{As4}$). Here, we investigated fractional fluxes between 1% and 10%, which corresponds to a range of Sb_2-BEP between 0.3×10^{-7} and 7.2×10^{-7} mbar. We assume the relatively small fractional Sb flux has almost no effect on the total V/III ratio. (ii) In a second series, we explored the effects of growth conditions (temperature and V/III ratio). A particular set of experiments is conducted where the V/III ratio is varied (~7–14) and the growth temperature tuned between 480 °C and 540 °C under fixed $FF_{Sb} = 6\%$ at a growth time of 1 h. The correlated data obtained from the two growth series was further used to realize optimized InAsSb NWs with high aspect-ratio with sufficiently large Sb incorporation.

All as-grown InAsSb NW samples were investigated by SEM to determine growth selectivity and yield, as well as NW morphology and aspect ratio (length/diameter). In addition, double-crystal HRXRD in a Philips X'Pert Pro MRD diffractometer was employed to determine the alloy composition (Sb-content) of the NW arrays via 2theta–omega (2θ–ω) scans. Further compositional and structural analysis was acquired by high-resolution (HR-) and STEM, as well as associated high-angle annular dark field (HAADF) Z-contrast imaging and EDXS, using a FEI Titan Themis TEM operating at 300 kV. Hereby, cross-sectional STEM analysis of the radial compositional structure was performed on ~100 nm thin lamellas prepared from the respective NW samples using focused ion beam (FIB).

3. Results and discussion

3.1. Role of Sb-flux on Sb incorporation and nanowire morphology

In a first set of experiments, we illustrate the dependencies of different Sb fractional fluxes (FF_{Sb}) on the NW morphology, aspect ratio, and effective Sb incorporation probed by SEM and HRXRD. Figures 2(a)–(f) show corresponding SEM images of InAsSb NWs grown with FF_{Sb} ranging from 0% to 10% at fixed growth temperature of 480 °C, V/III ratio of ~7, and growth time of 1 h (growth series (i)). The depicted micrographs are from arrays with identical mask opening diameter ($d_0 = 80$ nm) and pitch ($p = 0.5$ μm). Comparison amongst the individual arrays shows that in the SAE growth of InAsSb NWs by MBE the aspect ratio strongly declines with increasing FF_{Sb}, leading to reduced axial and enhanced lateral growth of the NWs. This trend reproduces very well many previous observations [12–14, 16–20], and confirms the anticipated Sb surfactant effect in III–V-Sb based NWs [19, 23–25, 35, 36]. A full quantitative analysis of the dependencies between Sb-flux and corresponding NW aspect ratio is summarized in table 1 and further shown below in relation to the different geometrical parameters (d_0, p).

Figures 2(g) and (h) depict further larger magnification SEM images in top view as well as 45° tilted view, to discern characteristic morphological differences between pure InAs NWs (g) and ternary InAsSb NWs (h). The InAs NWs exhibit a characteristic pencil-like shape with an inclined top facet
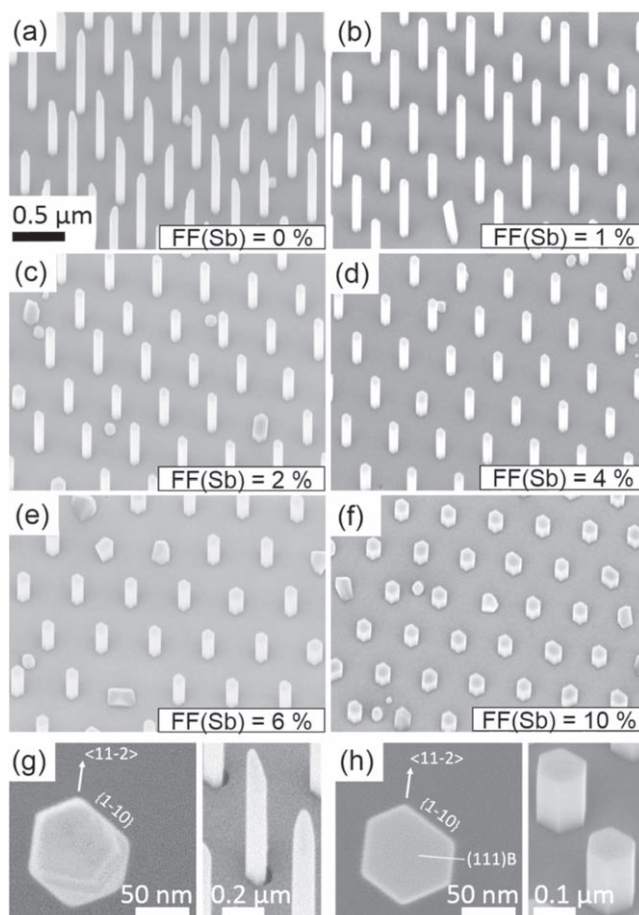

Figure 2. (a)–(f) Representative SEM images of periodic InAsSb NW arrays grown for 1 h with different FF_{Sb} ranging from 0% (InAs NWs) to 10%. Data shown here are for identical mask opening diameter $d_0 = 80$ nm and pitch $p = 0.5$ μm, and growth performed at 480 °C with a V/III ratio of ~7. The scale bar of 0.5 μm is identical for all images (a)–(f). The bottom SEM images illustrate the prevalent crystal orientations in top view (left) and the distinctly different NW morphologies in 45° tilted view (right) for InAs NWs (g) and InAsSb NWs ($FF_{Sb} = 2\%$) (h), respectively. Images in (g), (h) are taken from arrays with slightly larger mask opening diameter ($d_0 = 110$ nm) to demonstrate differences in nucleation and mask filling behavior between InAs NWs and InAsSb NWs.

structure. This type of top facet morphology is typical for catalyst-free [111]B-oriented InAs NWs grown by MBE from SiO_2 mask openings [31, 37, 38]. From the tilted-view image we also observe that the InAs NWs tend to nucleate at edge of the mask opening and, due to rapid vertical growth, do not overgrow the mask opening laterally, consistent with previous observations [31, 39]. Close-up view of the pencil-like shape in figure 2(g) evidences that the tip morphology is highly asymmetric, with the facets adjacent to the edge of the mask opening being longer than the facets facing the centre of the openings. Thus, we believe that the evolution of such asymmetric pencil-shape stems from slightly different effective material fluxes on the individual sidewall facets, given the non-centrosymmetric nucleation site geometry. Alloying InAs NWs with Sb may still lead to slightly asymmetric NW shape (see figure 2(h)), likely due to similar off-centered nucleation. Unlike the case of pure InAs NWs, however, the morphology

Table 1. Summarized data of NW dimensions (length L_{NW} and diameter D_{NW}) and mean XRD-measured Sb content x_{Sb} for different fractional Sb fluxes (FF_{Sb}) and corresponding beam equivalent pressure of Sb_2 species as obtained for growth series (i). The length and diameters are given as mean values (standard deviation) as derived from >20 NWs measured for each sample. The error in the Sb content represents the maximum uncertainty of the underlying crystal structure, i.e. WZ versus ZB phase.

FF_{Sb} (%)	BEP_{Sb} (mbar)	x(Sb) (%) [XRD]	L_{NW} (nm)	D_{NW} (nm)
0	0	0	704 ($\pm$90)	85 ($\pm$7)
1	0.3×10^{-7}	—	561 ($\pm$146)	92 ($\pm$8)
2	0.6×10^{-7}	6 ($\pm$2.8)	319 ($\pm$30)	93 ($\pm$3)
4	1.2×10^{-7}	11 ($\pm$2.8)	253 ($\pm$6)	100 ($\pm$5)
6	1.8×10^{-7}	20 ($\pm$2.7)	168 ($\pm$11)	109 ($\pm$11)
10	3.0×10^{-7}	25 ($\pm$2.7)	105 ($\pm$4)	145 ($\pm$12)

of the Sb-containing NWs remarkably resembles an almost perfect hexagonal prism. As seen in figure 2(b), even for small amounts of Sb (e.g. FF_{Sb} of 2%) the NWs exhibit equally long {1-10} sidewall facets throughout the entire NW. As a result, the top facet appears very flat and is mainly defined by an extended (111)B plane instead of inclined facets as in the case of InAs NWs. Although not specifically discussed before, such perfectly flat top facets are seen also in other growth studies of catalyst-free InAsSb NWs [8, 12, 17] and may be ascribed to the Sb surfactant effect. Hereby, under the influence of Sb the radial growth along the {1-10} facets is strongly enhanced, and, thus, the inclined planes at the NW tip (as present for InAs NWs) cannot develop as much, leaving behind a hexagonally shaped and flat (111)B plane at the top. Very similar observations were also made previously in catalyst-free InGaAs NW arrays, where the pencil-like tip structure and randomness in SiO_2 edge-nucleation were suppressed upon increasing the Ga-content [38], producing overall improved NW-array homogeneity. We note that despite the flat and well extended (111)B plane at the InAsSb NW growth front, there are still inclined, yet very small facets present towards the very edge of the NW top. We will see in the last section of this work, that these will play a role in creating a fairly complex radial compositional structure of the as-grown InAsSb NWs.

Figure 3(a) depicts 2θ–ω HRXRD scans of the periodic InAsSb NW arrays displayed in figure 2, which allow us to determine the alloy composition under the different Sb fractional fluxes FF_{Sb}. We note that besides the major Si (111) substrate peak ($2\theta = 28.44°$) and the composition-dependent InAsSb NW peak no other reflections are observed over even a larger 2θ-angle than depicted here. This directly confirms the perfect epitaxial relationship between the InAsSb NWs and Si, described by a coherent orientation of InAsSb [111] || Si [111]. As expected the respective InAsSb NW peak reflection shifts to smaller 2θ-angles with increasing Sb content, corresponding to an increase in the in-plane lattice parameter of InAsSb as shown in figure 3(b). To extract the alloy composition we use Vegards's law by linearly interpolating between the lattice constants of the binary constituents, i.e. InAs and InSb, and assuming that the epitaxial strain in the NWs is completely relaxed. Hereby, the Sb-content x_{Sb} is defined as the molar fraction of Sb replacing As atoms on group-V lattice sites. We note that the InAsSb NWs

are not phase pure and contain both WZ and ZB stacking (particularly for small Sb content), which complicates a precise extraction of the alloy composition. As a consequence, we employ Vegard' law to the limits of phase-pure WZ and ZB structure (via literature data [40]) and use the mean value as an estimate for the Sb-content x_{Sb} [41]. The maximum uncertainty in x_{Sb}, given by the phase-pure WZ versus ZB boundary conditions, is thereby $\pm$2.8% (for As-rich InAsSb NWs) that decreases slightly with increasing Sb content (see figure 3(b)). This illustrates that the WZ phase h(002) planes have a slightly smaller in-plane lattice parameter than the analogous c(111) planes in ZB phase. The mean values for x_{Sb}, are given in figure 3(a) for each HRXRD spectrum as well as by the solid datapoints in figure 3(b). Since our TEM investigations below confirm that the fraction of hexagonal h(002) stacking becomes very small for $x_{Sb} > 20\%$, we can describe the InAsSb NWs grown with the highest FF_{Sb} of 10% as being mainly ZB, which gives a Sb content as high as $\sim$28% instead of the underestimating mean value of 25%.

Under these conditions we find that the Sb content scales nearly linearly with the supplied FF_{Sb} for the given array geometry and within the range of investigated Sb fractional fluxes. Below we will further illustrate that this scaling law starts to fail for NW arrays with (i) differing geometrical parameters (pitch), and (ii) for FF_{Sb} larger than 10%. Figure 3(c) plots the NW aspect ratio as a function of the mean XRD-measured Sb content x_{Sb}, as extracted from a statistically relevant dataset of the SEM images of figure 2 (see table 1). Clearly, we observe an inverse relationship, indicating much smaller aspect ratio for increasing x_{Sb}. This behavior directly confirms the prevailing Sb surfactant effect that becomes more prominent towards higher Sb content [12–14, 16–20, 23–25]. The data also shows that under the present growth conditions and array geometry the aspect ratio drops even below 1, meaning the NWs have much larger lateral extension than along the vertical growth direction. In the next section we illustrate how the NW aspect ratio as well as Sb incorporation behavior can be further tuned by precise control of the array geometry parameters.

3.2. Dependency on array geometry parameters

One of the most significant effects of the array geometry parameters on the NW aspect ratio is given by the mask opening diameter d_0. Figure 4 depicts representative SEM
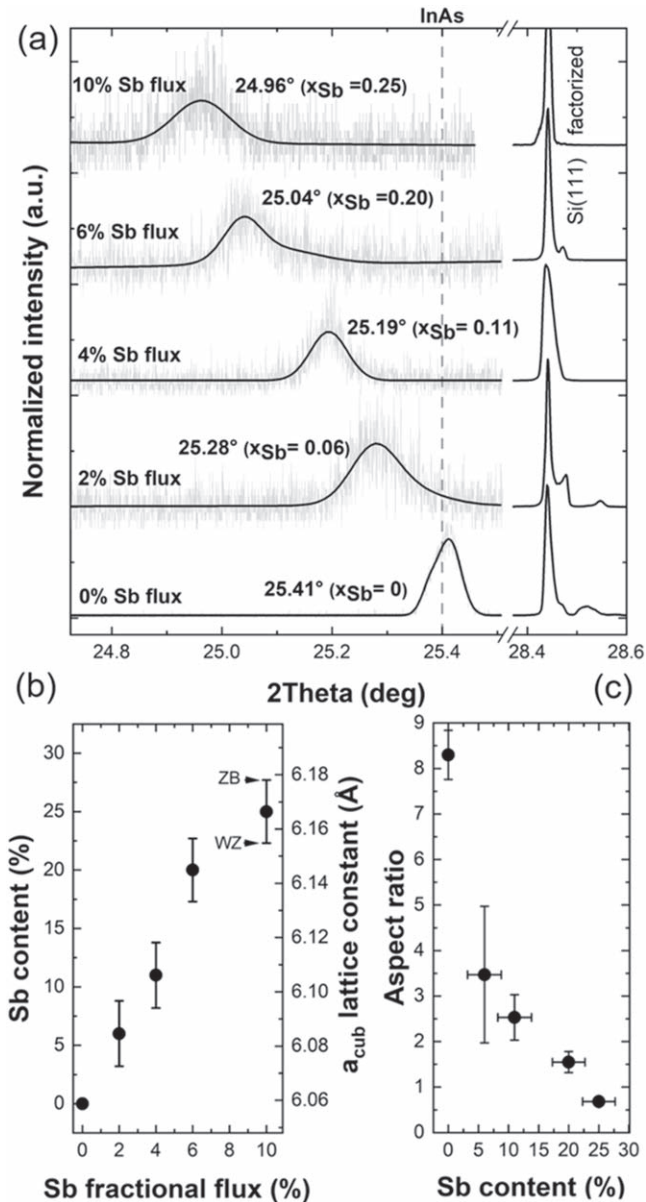
Figure 3. (a) HRXRD 2θ–ω scans recorded from the periodic InAsSb NW arrays shown in figure 2 for different Sb fractional fluxes (FF$_{Sb}$). The measured signal is shown in grey while curves in black are the cumulative peak fits to the data. The dashed line indicates the measured 2θ-peak position of binary InAs NWs used for linear interpolation of the actual Sb content x_{Sb} from the respective 2θ-peak positions of the InAsSb NW arrays via Vegard's law. (b) Dependence of the extracted Sb content x_{Sb} and in-plane lattice contstant a as a function of FF$_{Sb}$. The error bars account for the uncertainty in Sb-content under WZ- and ZB-related microstructure, while the data points give the mean value assuming equal fractions of WZ and ZB phase. (c) NW aspect ratio as a function of Sb content x_{Sb}. Error bars in aspect ratio stem from the size variation determined by SEM from >20 NWs/sample.

images of InAsSb NW arrays ($p = 0.5$ μm) for variable d_0 (30 nm, 80 nm, 150 nm), shown here for fixed FF$_{Sb} = 2\%$ and growth conditions as presented in the previous section (see figure 2). The NW yield in all arrays grown on mask openings with $d_0 > 60$ nm exceeds $\sim$90%, while it is lowered to $\sim$50% for openings as small as $d_0 = 30$ nm (figure 4(a)).
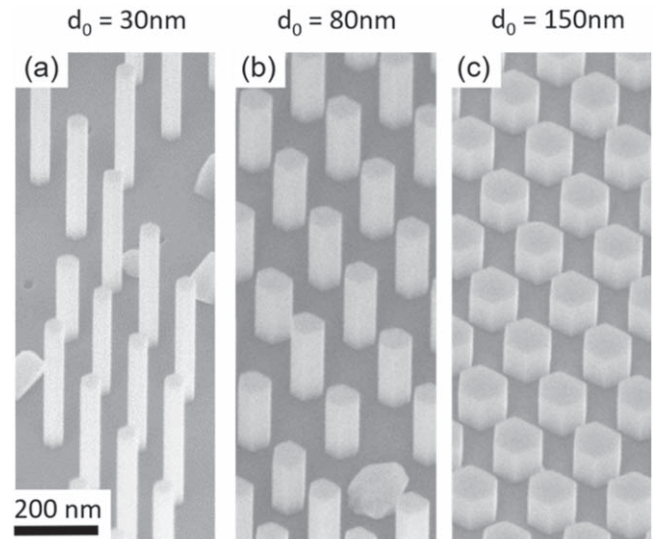

Figure 4. SEM images of InAsSb NW arrays (FF$_{Sb} = 2\%$, pitch $= 0.5$ μm) grown under conditions identical to those of figure 2, but for different mask opening diameters d_0 of 30 nm (a), 80 nm (b) and 150 nm (c). The scale bar of 200 nm is identical for all images.

This is most likely due to limiting factors in the EBL lithography process for size dimensions close to the resolution limit [42]. Most importantly, the data clearly shows an inverse dependency between NW aspect ratio and mask opening size, i.e. the NW aspect ratio increases strongly for growth from small mask openings. For example, we find an $\sim$8-fold increase in the aspect ratio for NWs grown from small openings ($d_0 = 30$ nm, figure 4(a)) compared to large openings ($d_0 = 150$ nm, figure 4(c)). Note, the changes in aspect ratio are evidenced by *both* the change in NW diameter and the inverse response in NW length with mask opening size, mimicking previously observed behavior in e.g. selective-area epitaxial GaAs NW arrays [43]. Hence, the inverse length-diameter dependence points towards an In-diffusion limited growth of the NWs where adatom diffusion on the sidewall facets is suppressed [44, 45]—a behavior that is further aggravated by the Sb surfactant effect as discussed below.

Interestingly, for the InAsSb NWs their diameter is always larger than the respective value of d_0, meaning that the NWs grow laterally beyond the defined mask opening (see figure 4). This is in contrast to pure InAs NWs grown under identical conditions, which exhibit diameters typically smaller than the mask opening size (at least for $d_0 > 80$ nm) (compare figures 2(g), (h)). As a result, the morphological evolution of InAs NWs does not follow the same scaling behavior with mask opening size as InAsSb NWs. Figure 5 plots the corresponding evolution of NW length, NW diameter and aspect ratio as a function of the mask opening diameter d_0 for different Sb fluxes (FF$_{Sb}$) in direct comparison to pure InAs NWs. The data directly shows that the NW diameter of InAs NWs increases only marginally from $\sim$75 to $\sim$120 nm when tuning d_0 from 20 to 150 nm. Likewise, the NW length remains nearly constant for a large range of d_0 ($\sim$80–150 nm) and increases only for very low d_0. Thus, the corresponding
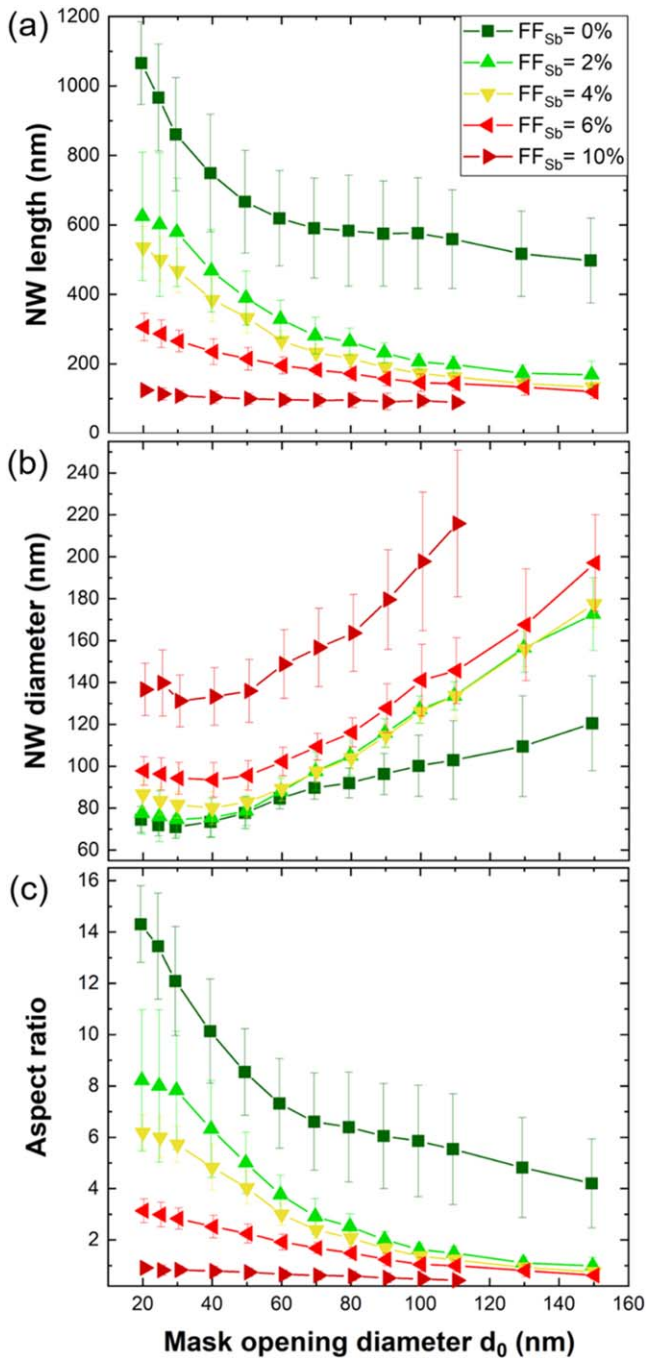
Figure 5. Evolution of NW diameter (a), length (b) and aspect ratio (c) as a function of the mask opening diameter d_0 for InAsSb NWs grown with different FF_{Sb} (0%, 2%, 4%, 6%, 10%). Error bars reflect the length and diameter dispersion obtained from a statistically relevant set of SEM measurements, i.e. 60 NWs per growth field.

aspect ratio of InAs NWs changes only by a factor of ~3 over the entire range of investigated mask opening diameters. This suggests that the growth dynamics of InAs NWs are mostly governed by the effective growth conditions rather than the mask opening size. For comparison, InAsSb NWs grown with even small FF_{Sb} of 2% exhibit much larger dependencies, i.e. the NW diameter increases from ~75 to ~155 nm while the NW length decreases from ~600 to ~150 nm for the

equivalent range of d_0 (=20–150 nm). Qualitatively similar dependencies with strongly increasing diameter and decreasing length are also found for other Sb fluxes, e.g. $FF_{Sb} = 4\%$ and 6%. Growth at very high FF_{Sb} of 10% finally leads to very short NWs with length of ~100 nm, where the effects of mask opening size variation become invisibly small. Still, the NWs exhibit a significant d_0 dependency with diameters changing from ~130 to ~220 nm over the entire range of d_0. The enhanced lateral growth and limited axial growth under such high FF_{Sb} corroborate clearly the underlying Sb surfactant effect.

Figure 6 presents the dependence of the NW morphology on the interwire spacing, exemplified by representative SEM images for three different pitches p between 0.25 and 1 μm. The selected InAsSb NW arrays are from the growth sample with $FF_{Sb} = 2\%$ and fields of fixed mask opening diameter of $d_0 = 80$ nm. The images evidence that the NW length increases slightly and saturates with increasing pitch. Interestingly, the NW diameter remains fairly unchanged over this relatively wide range of pitch. A more quantitative analysis was further performed for an even larger range of pitch (up to 2 μm) and for InAsSb NWs with different FF_{Sb}, as summarized in figure 7. Here, we confirm that the InAsSb NWs with $FF_{Sb} = 2\%$ exhibit an overall constant diameter of ~90 nm and only increase in length from ~250 to ~350 nm from $p = 0.25$ μm to $p = 1$ μm, while the length does not further increase towards $p = 2$ μm. A similar behavior is also found for InAsSb NWs grown with even higher FF_{Sb}. Despite the fact that the overall NW diameter increases with FF_{Sb}, the values for each sample are found to be nearly constant within the experimental error, irrespective of the selected pitch. Interestingly, the NW length saturates at gradually smaller pitch the larger the FF_{Sb} becomes, leading to completely constant NW length for the largest FF_{Sb} (10%) over the entire range of investigated pitches. In complete contrast, pure InAs NWs evidence a continually increasing length (from ~500 to ~850 nm) nm from $p = 0.25$ μm to $p = 2$ μm with no indication of saturation even at the largest pitch. Although less pronounced, the NW diameter also increases steadily from ~70 to ~90 nm with increasing pitch for InAs NWs.

To illustrate the combined effects of the NW length and diameter evolution with pitch more universally, we further plot the calculated volume of the NW (in units of μm^3) in figure 7(c). This allows us to probe the synergistic effects of surface diffusion and corresponding capture length scales of adatoms contributing to the effective incorporation and growth as a function of pitch and FF_{Sb}. Hereby, we employ the descriptions developed recently for various different NW systems [31, 46–49] which define two essential regimes of growth governed by the respective length scale differences between adatom migration on the SiO$_2$ mask layer (λ_{SiO_2}) and the pitch p. For example, if λ_{SiO_2} is on the order of or larger than half of the pitch ($\lambda_{SiO_2} > p/2$) then adjacent NWs in the periodic array compete for adatoms leading to a NW volume that strongly depends on pitch. This regime is commonly referred to as a rate-limiting *materials competition regime* [31, 46–49] and occurs typically for high-density NW arrays, i.e. small pitch (see figure 7(c)). As expected for this growth
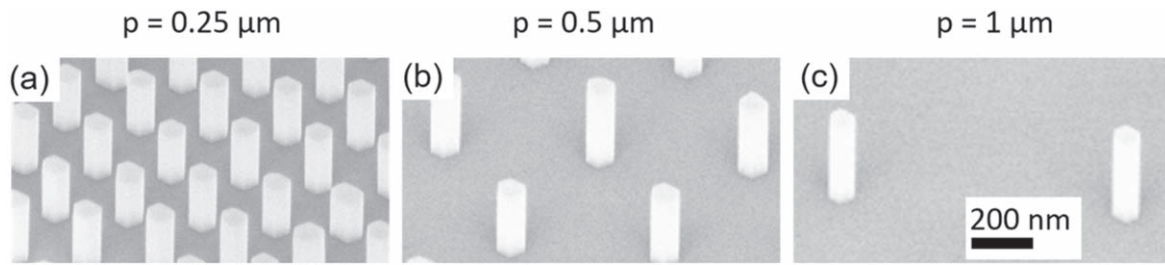
Figure 6. SEM images of InAsSb NW arrays ($FF_{Sb} = 2\%$, $d_0 = 80$ nm) for three different pitches p of 0.25 μm (a), 0.5 μm (b) and 1 μm (c), respectively. The scale bar (200 nm) is identical for all images. Growth conditions were again identical to those presented in all other previous figures.

regime, any slight increase in pitch yields a corresponding increase in the capture area for surface diffusing adatoms per individual NW, which in turn results in an increasing NW volume. This behavior is well reproduced for pure InAs NWs as well as low-Sb content InAsSb NWs ($FF_{Sb} = 1\%$), where the NW volume rises steadily at least up to a pitch that well exceeds $p > 1$ μm (figure 7(c)). In contrast, when the surface diffusion length λ_{SiO_2} is smaller than half the pitch, the NWs become largely independent of each other and do not compete for migrating adatoms. Thus, the growth and resulting NW volume is characterized by a *diffusion-limited regime*, where the volume does not change as a function of pitch anymore. In other words, only the adatoms arriving within a collection radius of around the NW that is defined by the given surface diffusion length can participate in the growth, whereas adatoms deposited outside the collection region desorb or form clusters on the SiO_2 surface [8]. This type of growth regime is well observed for all InAsSb NW arrays with larger FF_{Sb}, since the NW volume is fairly constant at least for a wide range of pitches ($\sim$0.25–2 μm). We note that in our case even for the largest FF_{Sb} hardly any parasitic clusters were found on the SiO_2, suggesting that adatoms outside the NW collection region desorb from the surface.

In general, the cross-over between the two respective growth regimes, i.e. the critical pitch at which the NW volume saturates, can be used to estimate the surface diffusion length λ_{SiO_2} under the given growth conditions. Obviously, the cross-over varies dynamically with the respective FF_{Sb} and shifts towards smaller pitches with increasing FF_{Sb} as indicated by the dashed lines in figure 7(c). For example, for InAs NWs and low-Sb content InAsSb NWs ($FF_{Sb} < 1\%$) the critical pitch occurs in between $\sim$1 and 2 μm, corresponding to an equivalent λ_{SiO_2} of $\sim$0.5–1 μm. This value is in good agreement with previously estimated surface diffusion lengths of In adatoms on SiO_2 masks under comparative growth conditions [31], suggesting that In adatoms are the primary species governing the observed growth dynamics due to their longer migration lengths over group-V species [29, 49, 50]. For higher Sb-content InAsSb NWs, the surface diffusion length of In adatoms is substantially reduced, e.g. for $FF_{Sb} = 2\%$ we obtain $\lambda_{SiO_2} \sim 0.3$–0.4 μm while for $FF_{Sb} > 6\%$ λ_{SiO_2} is only $\sim$0.15–0.2 μm, respectively (see figure 7(c)). This confirms that the presence of Sb strongly suppresses adatom migration not only on the NW sidewalls as

observed in figure 2, but also markedly on the growth substrate itself.

3.3. Effect of growth parameters on Sb incorporation and nanowire morphology

To further explore the growth dynamics in periodic InAsSb NW arrays we investigated the role of different growth parameters (V/III ratio, temperature, growth time) on the resulting Sb incorporation behavior and NW morphology with the aim to develop high aspect ratio NWs with high Sb content. First, we explore the variation of V/III ratio by changing the As_4 flux under fixed $FF_{Sb} = 2\%$, growth temperature of 480 °C and a growth time of 1 h. In particular, we doubled the V/III ratio from $\sim$7 (as used so far) to $\sim$14 (As_4-BEP $= 6 \times 10^{-6}$ mbar). According to recent data obtained for InAs NWs grown under very similar conditions [51], one expects a corresponding increase in the axial growth rate with As-flux (i.e. group-V limited regime). However, for Sb-containing InAs NWs this behavior is very different and depends further on the mask opening size d_0. Most importantly, for a wide range of $d_0 \sim$ 50–150 nm no change in NW length and diameter is found for arrays grown at V/III $\sim$ 7 and V/III $\sim$ 14, respectively (not shown). In other words, the NW aspect ratio is governed by the mask opening size only and follows the same trends found in figures 4 and 5, irrespective of the V/III ratio. This behavior is similar to observations by Potts *et al* [17], who observed only a measurable V/III-ratio dependent change in the NW aspect ratio at low As_4-BEP whereas for As_4-BEP $> 3 \times 10^{-6}$ the aspect ratio tends to saturate. This suggests that in the limit of high V/III ratio and intermediate to large d_0 the Sb surfactant effect is enhanced, such that growth is occurring rather in a group-III limited regime in which the aspect ratio remains unchanged under varying V/III ratio [51]. Surprisingly, however, for $d_0 < 50$ nm we find an enhancement in aspect ratio upon increasing V/III ratio. For example, at $d_0 = 30$ nm, arrays with $p = 0.5$ μm and V/III ratio of 14 yield $\sim$700 nm long NWs while they are only $\sim$450 nm long for a V/III $\sim$ 7, despite comparable NW diameters. As will be further verified in the next section, the increased axial growth rate under these conditions is a key parameter to increase aspect ratio and also Sb incorporation.

Another very interesting dependency is observed by changing growth temperature. Figure 8 depicts SEM images
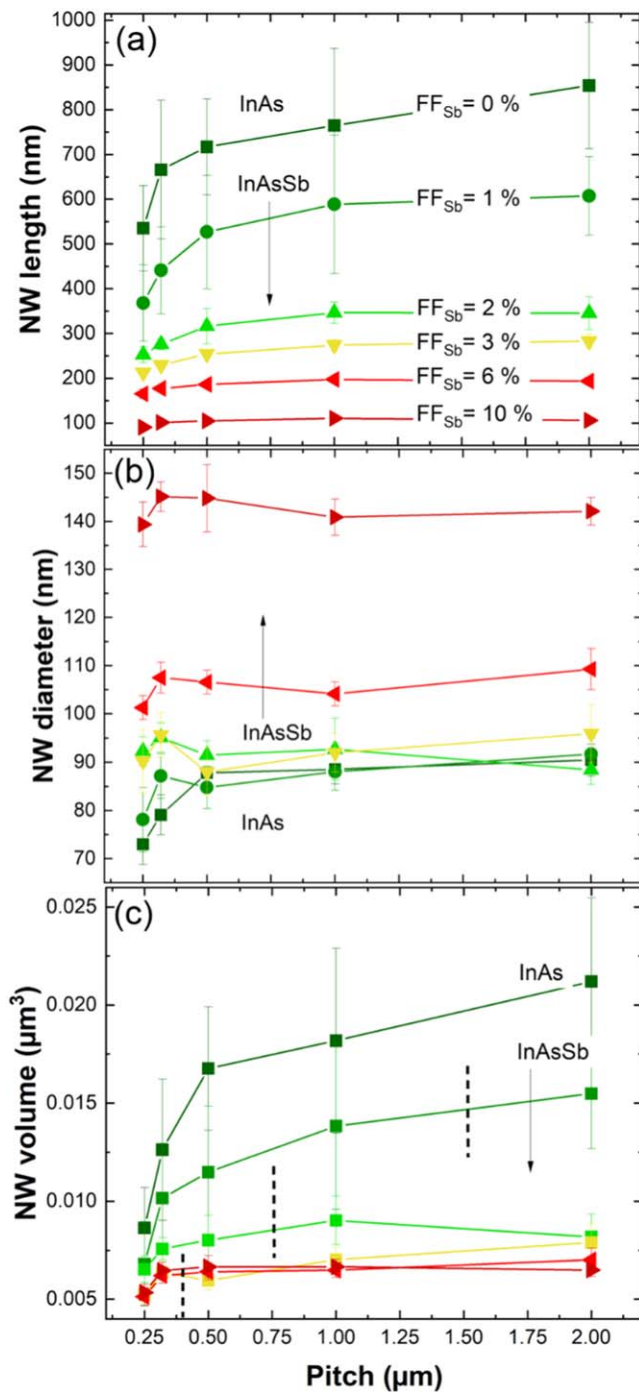
Figure 7. Dependence of the NW length (a), diameter (a), and average volume per NW (c) on the pitch p for InAsSb NWs grown with different FF_{Sb} (0%, 1%, 2%, 3%, 6%, 10%). The dashed lines in (c) mark the cross-over from the materials competition regime ($\lambda_{SiO_2} > p/2$) to the diffusion-limited regime ($\lambda_{SiO_2} < p/2$) for different FF_{Sb}.

of InAsSb NW arrays ($p = 0.5$ μm, $d_0 = 80$ nm) grown under fixed conditions (i.e. V/III ratio ~ 7, $t = 1$ h, $FF_{Sb} = 6\%$) but variable growth temperatures between 480 °C and 540 °C (growth series (ii)). We clearly observe a characteristic increase in NW length and aspect ratio upon increasing temperature, i.e. the aspect ratio of ~ 1.5 for InAsSb NW grown at 480 °C rises to >6 for NWs grown at

540 °C (see also table 2). Simultaneously, the NW yield decreases with increasing temperature as seen in figure 8. In addition, the relative increase in aspect ratio with temperature is found to be much more pronounced for smaller mask openings compared to large openings (not shown). For example, for $d_0 > 100$ nm the aspect ratio changes by less than $\sim 50\%$ for a temperature increase between 480 °C and 520 °C, while for $d_0 < 60$ nm it is increased by nearly $\sim 250\%$ over the same temperature range. We believe that two effects contribute to the overall increase in aspect ratio with temperature: first, at higher growth temperature the collection radius of surface diffusing adatoms on the SiO_2 increases, resulting in an increased effective material supply at the NW sites. Secondly, surface diffusion on the NW sidewall facets is enhanced at higher temperature, which leads to a rise in the axial NW growth rate. In fact, this behavior mimics closely recent observations seen in both InAs NWs [51] as well as InAsSb NWs [8, 17] grown by both MBE and MOCVD.

Another important effect to be considered is the inhibition of the Sb surfactant effect, especially as less Sb may be incorporated in the limit of high temperature growth. While the effects of Sb incorporation on growth temperature have been well established for planar growth [52, 53], relatively little data exists for InAsSb NWs. A first indication of a reduced Sb incorporation in InAsSb NWs at higher growth temperature is noted by Sourribes *et al* [16] by comparing growths at two temperatures. Based on this, we provide a more systematic study of the Sb incorporation over a temperature range of 480 °C–520 °C using HRXRD. Figure 8(e) shows 2θ–ω HRXRD scans of the InAsSb NW arrays as displayed in figures 8(a)–(d) for a fixed $FF_{Sb} = 6\%$ and pitch $p = 0.5$ μm. From the respective InAsSb NW peak reflections we note that increasing the growth temperature yields indeed the expected decrease in the Sb content x_{Sb}, however, not in a continuous manner. For example, NW arrays grown at 480 °C and 500 °C exhibit peak reflections at nearly identical 2θ-angle, resulting in a x_{Sb} of $\sim 20\%$–21% (i.e. mean value under the assumption of mixed ZB/WZ phase). Only for growth at 520 °C the Sb content starts to drop to $x_{Sb} \sim 15\%$, while the array grown at 540 °C produced insufficient XRD signal due to the relatively poor yield. A further interesting relation is found between the array spacing and resulting alloy composition when grown at different temperatures. Figure 8(f) plots HRXRD spectra for InAsSb NWs grown in arrays of lower pitch $p = 0.25$ μm, but under otherwise identical conditions as those of figure 8(e) ($p = 0.5$ μm). Direct comparison evidences that NW arrays exhibit substantially lower Sb content when the array spacing is decreased. Specifically, the Sb content was decreased by as much as $\sim 5\%$–6% in arrays with $p = 0.25$ μm, as confirmed by two sets of InAsSb NW arrays grown at 500 °C and 520 °C. This suggests that the Sb incorporation is not self-limiting and that it follows the kinetics of growth in the materials competition regime typical for low to intermediate array spacings. Thereby, the Sb diffusion on the underlying SiO_2 mask must be sufficiently large as the NWs capture and incorporate increased amount of Sb when the pitch increases. We thus assume that the Sb diffusion exceeds p(500 nm)/
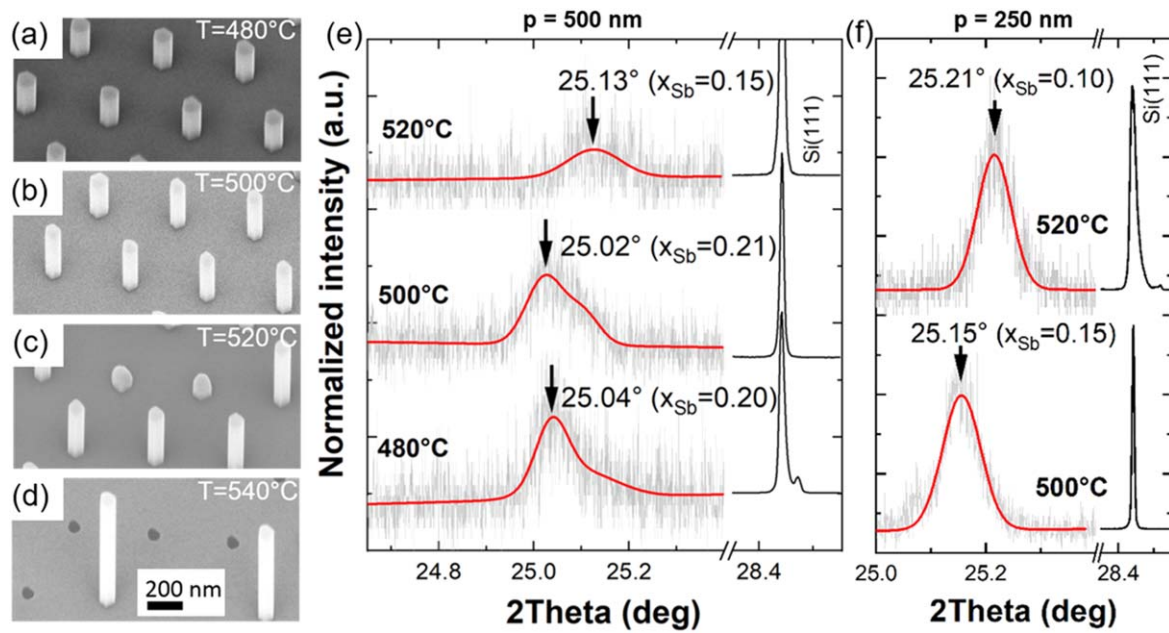
Figure 8. SEM images of InAsSb NW arrays ($FF_{Sb} = 6\%$, $d_0 = 80$ nm, $p = 0.5$ μm) grown for 1 h under V/III ratio $\sim$7 at four different temperatures of (a) 480 °C, (b) 500 °C, (c) 520 °C, and (d) 540 °C. The scale bar (200 nm) is identical for all images. (e), (f) HRXRD 2θ–ω scans recorded from periodic InAsSb NW arrays grown under different temperature at fixed $FF_{Sb} = 6\%$ for an array spacing, i.e. pitch of $p = 0.5$ μm (e), and a pitch of $p = 0.25$ μm (f) for comparison.

Table 2. Growth temperature and pitch dependence on the resulting NW dimensions (length L_{NW} and diameter D_{NW}) and the mean XRD-measured Sb content x_{Sb} for InAsSb NW arrays grown under fixed conditions ($FF_{Sb} = 6\%$, V/III = 7, $t = 1$ h, and $d_0 = 80$ nm). The average length and diameters as well as their standard deviation are derived from a statistical SEM analysis of >20 NWs measured for each sample.

T (°C)	Pitch (μm)	L_{NW} (nm)	D_{NW} (nm)	x(Sb) (%) [XRD]
480	0.5	168 ($\pm$11)	99 ($\pm$2)	20 ($\pm$2.7)
500	0.5	257 ($\pm$6)	94 ($\pm$2)	21 ($\pm$2.7)
500	0.25	240 ($\pm$22)	88 ($\pm$2)	14 ($\pm$2.8)
520	0.5	281 ($\pm$21)	96 ($\pm$2)	15 ($\pm$2.8)
520	0.25	266 ($\pm$24)	92 ($\pm$3)	10 ($\pm$2.8)
540	0.5	597 ($\pm$65)	94 ($\pm$2)	—

$2 > 250$ nm, which is reasonable given the ready diffusion properties of Sb [23, 54] and the higher temperature growth conditions. This finding demonstrates that accurate control of the interwire spacing is very critical for the resulting alloy composition of ternary III–V-Sb NW arrays, and that non-periodic growth from spatially random positions most likely produces large fluctuations in composition across the growth sample [26].

3.4. Structural properties in optimized high-aspect ratio InAsSb nanowires

Employing the extensive knowledge gained from the growth kinetics and geometrical array parameter studies, we created optimized InAsSb NW arrays with high aspect ratio and sufficiently large Sb incorporation. Hereby, we performed an additional growth experiment with optimized growth parameters using a growth temperature of 520 °C and V/III ratio = 14. The array geometrical parameters were set to $p = 0.5$ μm and a small mask opening diameter $d_0 = 50$ nm, which are key to high-aspect ratio NWs and enhanced Sb incorporation. Figure 9(a) exemplifies a typical SEM image of high-aspect ratio InAsSb NWs as obtained for growth using relatively high $FF_{Sb} = 6\%$ (sample A). For a growth time of 2 h, the NWs on average are $\sim$1.9 μm long and exhibit a diameter of $\sim$135 nm, yielding a high aspect ratio of $\sim$14. The corresponding Sb content as measured by HRXRD amounts to a mean $x_{Sb} = 24\%$ ($\sim$27% assuming ZB-phase). We suggest that the increased growth rate reduces the Sb surfactant effect, and thus leads to increased Sb content, which is in agreement with observations in planar InAsSb films [55]. In addition, another sample with very high $FF_{Sb} = 12\%$ (sample B) was grown to investigate the limits of Sb incorporation under the otherwise same growth conditions. As expected from our previous studies, the average length decreased to $\sim$750 nm with an average diameter of $\sim$150 nm. Despite doubling FF_{Sb}, the Sb content for this sample as measured by HRXRD amounts only to a mean $x_{Sb} = 28\%$ ($\sim$31% assuming ZB-phase), indicating a saturation of the Sb incorporation under these conditions.

High-resolution (HR-) and STEM was further performed to characterize the microstructural and compositional properties of individual NWs. The TEM experiments were performed on NWs transferred from the optimized growth sample (sample A) onto a carbon-coated copper grid and probed in a FEI Titan Themis operated at 300 kV. Hereby, both diffraction patterns and HR-TEM images were recorded in a $\langle 110 \rangle$ zone axis corresponding to the side facets of the NWs. For the TEM analysis the size of the selected area
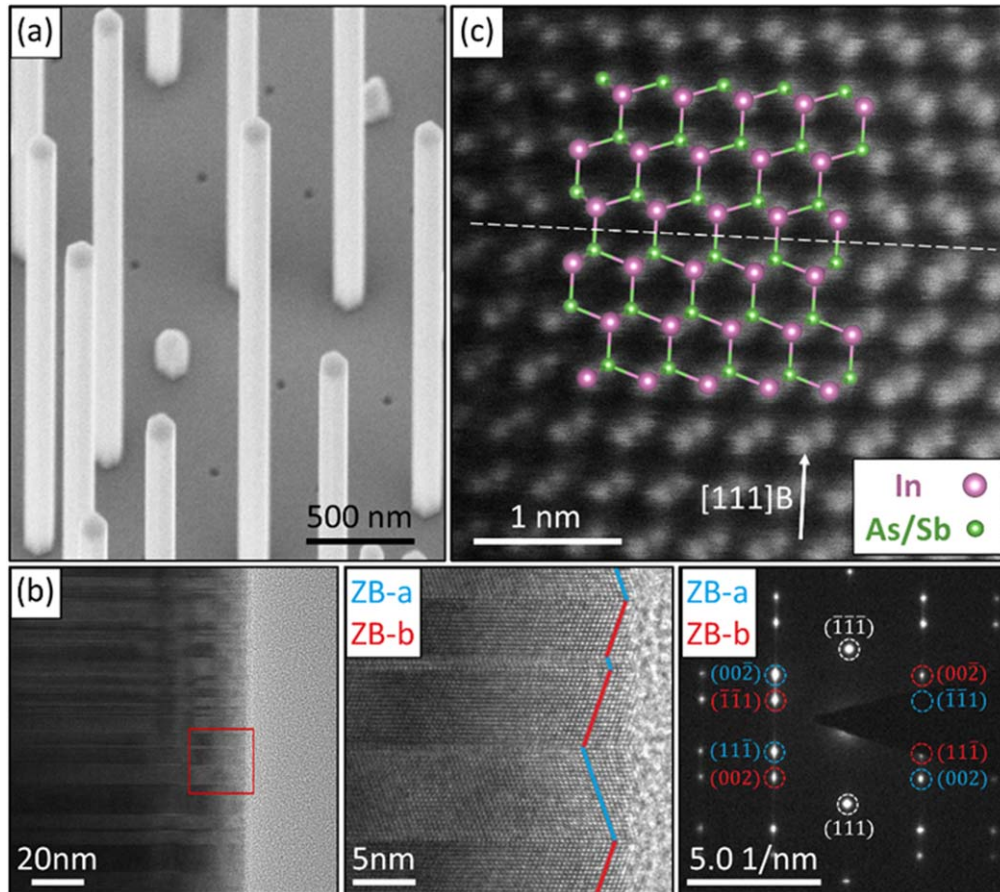
Figure 9. (a) SEM image of high aspect-ratio InAsSb NWs (sample A: $FF_{Sb} = 6\%$, $x_{Sb} = 24\%$ (27% under ZB phase)) resulting from optimized growth conditions (as described in the text) and array geometrical parameters of $p = 0.5$ μm and $d_0 = 50$ nm. (b) (Left) Representative TEM micrograph of a single NW from the same array taken in the central part along the growth axis. (Center) High-resolution TEM micrograph recorded in a region marked by the red box. The alternating stacking between ZB-a (blue) and ZB-b (red) domains is directly illustrated. (Right) Corresponding SAD pattern evidencing that the NW contains only ZB structure with rotational twin defects (indexed by ZB-a and ZB-b domains). (c) High-resolution STEM image of a small section of the same InAsSb NW around the vicinity of a single rotational twin defect recorded along the $\langle 110 \rangle$ zone axis. The schematic of the InAsSb ZB crystal structure illustrates In atoms (purple) and As/Sb atoms (green) and their ABC stacking, which is mirrored (rotated by 60°) by the twin plane boundary (dashed line).

diffraction (SAD) aperture was adjusted to the full length of the NW to gain representative diffraction pattern information of the whole NW. Figure 9(b) (left image) illustrates a typical TEM image obtained from a single NW close to one of the side facets. The NW exhibits contrast modulations along the vertical growth axis, which are associated with rotational twin-plane domains as verified by the higher-resolution TEM image (figure 9(b), center), the corresponding SAD pattern (figure 9(b), right) as well as the HR-STEM image in figure 9(c). In particular, the SAD pattern captures the crystal structure of the whole NW and shows reflections that are exclusively assigned to rotational ZB-domains (ZB-a, ZB-b), marked in blue and red, respectively. For comparison, reflections marked in white are identical for both types of ZB domains and do not discriminate between ZB and WZ structure, e.g. the ZB-(111) reflection is identical to the WZ-(002) reflection. Furthermore, reflections that are sensitive to WZ structure (e.g. the $1\bar{1}2$ and $\bar{1}12$-type reflections [56]) would be positioned intermittently between ZB-a and ZB-b reflection pairs, and are found to be absent in the SAD pattern. Based on a statistically relevant analysis of SAD patterns

as well as HR-TEM images taken from multiple NWs, we never observe WZ phase in these high-Sb content InAsSb NWs but overall ZB-phase with a large number of rotational twins. The twin defect density was counted from HR-TEM images taken at several sections along the same as well as other NW and amounts to an average of $\sim 220 \pm 60$ μm^{-1}. The longest phase-pure ZB-domain was approximately ~ 20 nm, corresponding to ~ 54 layers along the (111)-plane. For comparison, we also examined InAsSb NWs with lower ($x_{Sb} = 13\%$) and higher Sb-content ($x_{Sb} = 31\%$, sample B) as well as NWs without any Sb, grown under similar conditions (not shown). Both the low and high-Sb-content InAsSb NWs exhibit qualitatively very similar microstructure, i.e. ZB phase with rotational twin domains, and a trend towards reduced twin defect density with increasing Sb-content (e.g. $\sim 105 \pm 20$ μm^{-1} for $x_{Sb} = 31\%$, sample B). In contrast, catalyst-free InAs NWs grown under comparable V/III ratio and temperature are dominated by a WZ-phase with a very high density of stacking faults [27, 41, 56, 57]. We note that the phase transition from predominant WZ to ZB phase upon alloying InAs NWs with Sb mimics closely previously

observed behavior reported by other groups [13–18], and confirms the theoretical trend based on the very low ionicity of the atomic bonds in Sb-containing InAs NWs [21]. Also, our twin defect density data compares fairly well with those reported in VS-grown catalyst-free InAsSb NWs in the low-to-intermediate Sb-content regime ($x_{Sb} \sim 10\%$–25%) [16, 17]. For higher Sb content, however, only few reports exist regarding catalyst-free InAsSb NWs, which suggest the complete suppression of twin defects and formation of phase-pure ZB InAsSb NWs at threshold Sb content near $x_{Sb} \sim 25\%$ [17]. Our results on the high Sb-content NWs ($x_{Sb} \sim 27\%$ (ZB, sample A) and $x_{Sb} \sim 31\%$ (ZB, sample B)) cannot confirm this observation, suggesting that the critical Sb-content for creating phase-pure ZB InAsSb NWs is not universal and most likely depends on the growth kinetics (e.g. temperature, V/III ratio).

Further evidence of isolated twin defects and their atomic structure are represented in figure 9(c) by the high-resolution STEM image taken on sample A along the $\langle 110 \rangle$ zone axis, with the $\langle 111 \rangle$ growth axis pointing upwards. As recorded via an HAADF (high-angle annular dark field) detector, the image clearly resolves the individual atomic bilayer rows of group-V/group-III element dumbbells along the growth direction. One of the two atom columns of each dumbbell shows higher contrast and is slightly larger, which indicates that the respective atomic number (Z) is higher [58]. Since the fraction of Sb in the NW is $\sim 27\%$, the average Z-number of the As/Sb rows is ~ 42 ($Z(As) = 33$, $Z(Sb) = 51$), while that of In constituents amounts to 49. Therefore, the larger and brighter atom columns represent the In columns and the smaller ones the columns of As/Sb, respectively, while we cannot discriminate between either As or Sb atoms. To better illustrate this, we overlaid the consecutive atomic bilayers in the STEM image by the schematic color-coded ZB crystal structure (see inset) i.e. the larger In atoms are depicted in purple and smaller group-V constituents (As/Sb atoms) in green. From this we directly see that the upper atoms of the bilayer rows are composed of group-V elements (As/Sb), which confirms that the growth direction of the InAsSb NWs in the $\langle 111 \rangle$B orientation [58]. The image as well as the schematic also directly reflect the ZB-type 'ABCABC' stacking, whereas an individual twin-plane boundary (marked by the dashed line) induces a mirror image of the layer stacking, i.e. 'C′B′A′C′B′A′' by a rotation of $60°$.

3.5. Compositional structure of SAE-grown InAsSb nanowires

Additional interesting results were obtained from systematic cross-sectional analysis of the InAsSb NWs, providing insights into the microscopic compositional structure and alloy ordering phenomena in the NWs. Hereby, NWs from sample A as in figure 9 as well as NWs from sample B were mechanically transferred from the growth substrate to a Pt-coated Si substrate for FIB preparation of TEM specimen. Well-aligned NWs were selected in SEM mode (i.e. seven NW (sample A)/three NWs (sample B) as shown in figure 10(a)), which were further embedded in ~ 200 nm thick carbon protection layer (deposited by electron beam induced

deposition in a Zeiss NVision 40 FIB-SEM) and a second protective platinum matrix fabricated by ion beam deposition at 30 kV, in order to reduce electron and ion beam induced damage of the sample during FIB preparation. Subsequently, a FIB-lamella was cut by the Ga-ion beam in a direction perpendicular to the growth direction of the NWs. The FIB cut was performed at a position that allows to probe a statistical variation of cross-sections that originate from either the middle region or near one end of the NW (see yellow line in figure 10(a)). The prepared lamellas have a thickness of ~ 100 nm, and sections of the main regions of interest are shown by the low-magnification STEM-HAADF (high-angle annular dark field) images in figure 10(a) for the two samples, respectively. The images, recorded along the [111] zone axis, clearly illustrate the hexagonal cross-sections of the different NWs and further shows the protective layers surrounding the NWs.

Figure 10(b) presents image-contrast enhanced, high-resolution STEM-HAADF (Z-contrast) images of selected cross-sections obtained from two representative NWs of sample A and sample B, respectively. Interestingly, all the depicted images evidence a non-uniform InAsSb alloy distribution due to slight variations in Z-contrast in the radial direction. In particular, they exhibit an *unintentional* core–shell like structure characterized by a core and shell (bright contrast) which are separated by a faint coaxial boundary layer and six bands along the {11-2} corner facets in slightly darker contrast. Obviously, the formation of the core–shell like structure and the respective dimensions of the individual layers depend sensitively on the position along the NW axis at which the cross-section was fabricated. For example, in NW-A#7 (cut very close to NW bottom) the core is smaller in size while it is more extended in NW-A#1 (cut closer to NW center). Analogous behavior is also found in NWs from sample B, e.g. NW-B#1 cut towards the NW tip exhibits a very extended core, whereas its size is reduced when cut near the NW center (NW-B#2). A striking feature of the core–shell structure is that the radial evolution in alloy composition is not continuous, but is obviously disrupted by a discontinuous coaxial boundary layer, at which the six corner bands emerge and propagate to the surface. We note that similar observations of such an unintentional core–shell structure were made in several other ternary III–V NW systems (including InAsSb NWs [17]), primarily though in NWs grown by the VLS growth mode [59–63]. In the case of VLS-grown NWs, it is argued that the unintentional shell forms due to parasitic VS growth concurrently to the dominant axial VLS growth [59–63], resulting in an alloy composition different than in the core.

To closely identify the nature of the compositional structure for the present catalyst-free InAsSb NWs, which are grown entirely in a VS-regime, we performed correlated chemical analysis of the alloy composition using EDXS. Corresponding EDXS elemental maps of the group-V species (As, Sb) are depicted in figure 10(c), as recorded from representative regions of interest of the two specific NW cross-sections (marked by boxes in figure 10(b)). The maps clearly confirm that the core–shell like structure and the
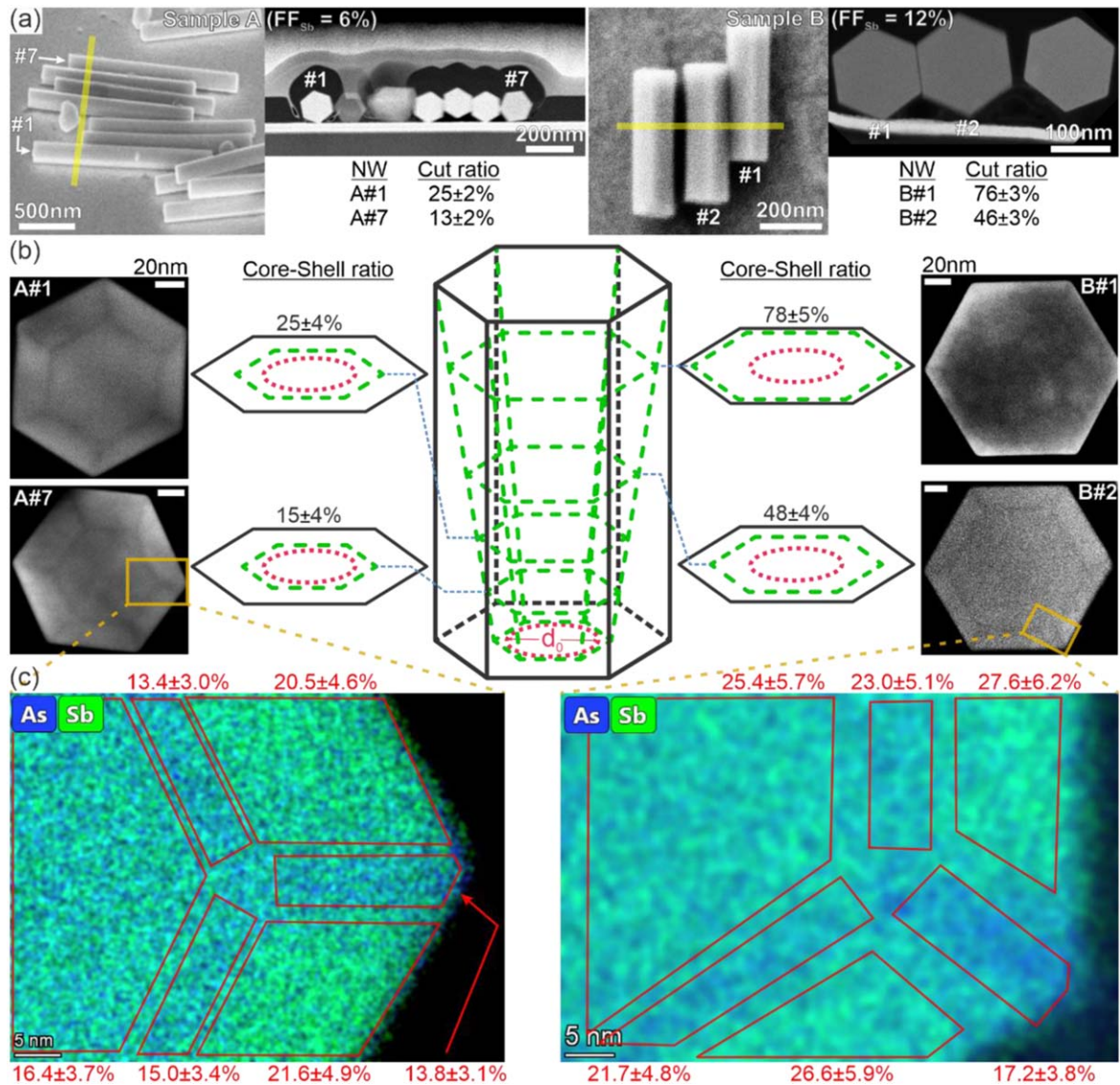
Figure 10. (a) SEM images of InAsSb NWs (sample A same as in figure 9; sample B same growth conditions as sample A but doubled FF_{Sb}) transferred to a Pt-coated Si substrate from which ∼100 nm thick lamellas were cut perpendicular to the NW axis (yellow line) on a set of seven/three well-aligned NWs using FIB. Low-resolution STEM-HAADF overview images of the individual FIB-cut lamellas, showing the cross-sections of the seven/three NWs next to each other along the [111] projection, respectively. The cut ratio is determined from the SEM images by relating the position of the FIB cut to the total length of each nanowire. (b) Contrast-enhanced high-resolution STEM-HAADF images of selected NWs evidencing the formation of an unintentional core–shell structure; i.e. a Sb-deficient hexagonal ring inside each NW in conjunction with Sb-deficient stripes along ⟨11-2⟩ between the corners of the inner hexagon and the corners of the NW surface. The core–shell ratio is determined by the fraction of the diameter of the inner hexagon (minus mask opening diameter d_0) and the diameter of the whole nanowire (minus d_0). (c) Corresponding EDXS maps on the selected NWs from representative regions of interest (marked by yellow boxes in (b)), illustrating the radial compositional distribution of group-V elements (As/Sb). The Sb molar fraction (x_{Sb}) as determined by EDXS quantification of specific areas of interest (outlined in red) of the core–shell structure are noted outside the maps in red. In both samples, we observe a clear increase of x_{Sb} in the shell compared to the inner core and a distinct Sb-deficiency at the interface between core and shell and along the ⟨11-2⟩ corner directions.

additional stripe features/bands at the corner facets arise from non-uniformities in the molar fractions of As and Sb species. For accurate determination of the Sb molar fraction in every region of interest, we corrected for systematic quantification errors (especially different absorption of the As-K peaks at higher energies compared to the In-L and Sb-L peaks at lower energies) by normalizing the ratio of group III elements to group V elements to 50:50. Using this correction, quantitative EDXS analysis performed on a section of NW-A#7

demonstrates that the outer shell exhibits the highest Sb-content with $x_{Sb} \sim 21\%$, the inner core shows an intermediate $x_{Sb} \sim 16\%$, whereas the Sb-content is lowest in the ∼3–4 nm thin coaxial layer and the six bands along the corner facets, i.e. $x_{Sb} \sim 14\%$ on average. Similar quantitative behavior given by a high Sb-content shell, an intermediate Sb-content core and low x_{Sb} in the boundary layers is also found for NW-B#2, although the Sb-deficiency in the coaxial layer is less pronounced. We note that on average the EDXS-measured

Sb-content is generally lower than that determined by HRXRD. We attribute this deviation to the challenging EDXS signal fitting [64] of the partially overlapping characteristic L-α and L-β lines of In and Sb.

To explain the observed compositional structure, we discuss in the following considerations based on existing literature as well as propose a hitherto undiscussed model scenario for the decomposition of ternary III–V NWs into the unintentional core–shell structure. For III-As-Sb ternary NWs it is commonly assumed that due to the different chemical potentials of the major {1-10} sidewall and minor {11-2} corner facets, As and Sb adatoms tend to diffuse towards the {1-10} facets [65, 66]. Since the Sb diffusion length is generally larger than that of As [23, 54, 67, 68], the six {11-2} corner facets at the intersection of the {1-10} sidewalls form Sb-deficient bands, resulting in Sb-antisegregation layers [17, 62]. In contrast, the formation of the discontinuous boundary layer has remained puzzling. Previous studies have dismissed the dark boundaries in STEM-HAADF images as artefacts due to strain between core and shell [17]. Our EDXS maps, however, clearly show that these boundary regions actually stem from a real depletion in Sb-content. Like for the six {11-2} corner facets, the systematically lower Sb-content in the coaxial boundary layer, hints thus to the presence of additional crystallo-graphic growth facets and corresponding anisotropies in adatom diffusion and bonding preferences [69, 70]. Actually, the discontinuous coaxial boundary layer seems to be universally occurring in many continuously-grown ternary NW materials, including AlGaAs [71], InGaAs [61], GaAsSb [61], InAsSb [17], and GaAsP [63] NWs. Recently, de Lepinau *et al* [63] explored several different factors that may originate in the distinct coaxial boundary layer (such as e.g. local strain, growth kinetics, growth flux geometry, segregation at triple phase line in droplet-induced NW growth, etc)—however, so far, no conclusive statement about the origins could be made.

We propose that, similar to the {11-2} corner stripes, the occurrence of the thin Sb-deficient coaxial boundary layer can be explained via a nanoscale facet that forms at the corner of the intersection between the (-1-1-1) top facet and the {1-10} side wall facets. Indeed, we can directly test this hypothesis by correlating the position of the FIB-cut with the position of the coaxial boundary layer. By assuming the top (-1-1-1) facet and (1-10) side wall growth rate to be approximately constant during NW growth, we can model the position of the boundary layer to be linearly dependent on the position along the NW (figure 10(b)). In this model, when looking at a cross-section close to the nucleation site, the diameter of the inner hexagonal core should be closely related to the initial mask opening diameter d_0 and propagate outwards the closer the cut gets toward the other end of the NW. In case the model is a good approximation for the growth behavior, the 'cut ratio' (as calculated by taking the ratio of the position of the cut to the total NW length) and the 'core–shell ratio' (as calculated by $(d_{BL} - d_0)/(d_{NW} - d_0)$, with d_{BL} being the diameter of the boundary layer and d_{NW} the diameter of the total NW) should be strongly correlated. Indeed, the results of these calculations match very closely within the experimental errors given by
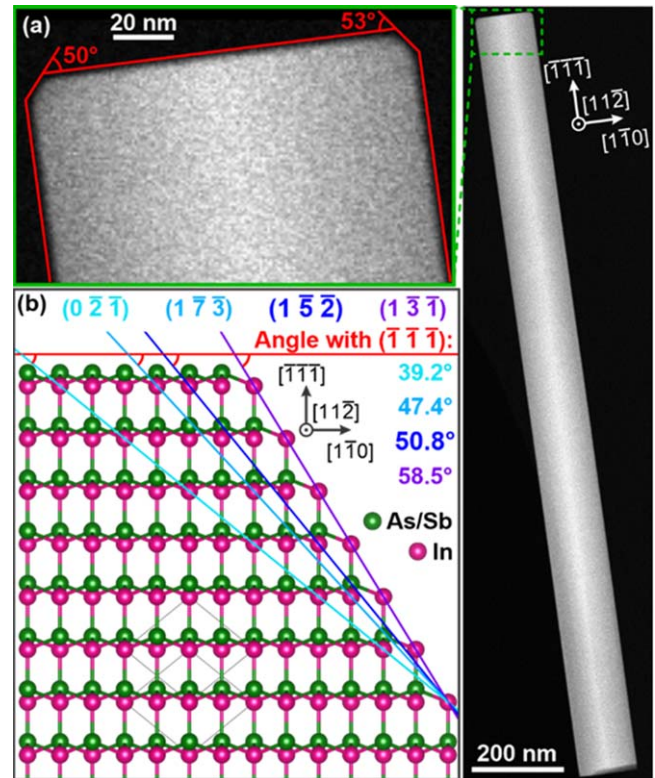

Figure 11. (a) Low resolution STEM-HAADF image of InAsSb NWs (sample A as in figures 9 and 10) with magnified view of the top end segment. At the intersection of the (-1-1-1) top facet and the (1-10) side facets, nanoscale truncations are observed and the truncation angle determined to be ∼50° on one side and ∼53° on the other side (uncertainty of about ±5° due to low resolution). (b) Cut-away atomic model of the ZB crystal, oriented in a geometry corresponding to the InAsSb NW direction. Several low index facets nearby the observed truncations are delineated. The theoretical angle of 50.8° for the (1-5-2) facet best fits our observations, although the occurrence of other nearby facets like (1-3-1) or (1-7-3) cannot be completely ruled out due to uncertainty.

measurement uncertainties (e.g. due to slight core–shell asymmetries) and statistical size fluctuations of d_0 (see figures 10(a), (b)). We suggest that the coincidence between calculated and measured data could be even further improved when the core–shell structure is perfectly symmetric.

In order to further illustrate the origin of the boundary layer, we investigated the intersection of the top facet with the sidewall facets by imaging with STEM in ⟨11-2⟩ zone axis (figure 11(a)). Hereby, we observe truncations at the corners with angles around ∼50–53°. By looking at an atomistic model of the ZB crystal in this zone axis (figure 11(b)) we try to identify low index facets which could be associated with the truncation and, therefore, the origin for the hexagonal Sb-depletion boundary layer. Of the several investigated facets, i.e. (0-2-1), (1-7-3), (1-5-2) and (1-3-1), the theoretical angle of 50.8° between the top (-1-1-1) and truncated (1-5-2) facet matches our observations most closely. However, based on the large measurement error of ±5° due to image resolution, we cannot unambiguously exclude the other possibilities and hence the exact facet is difficult to pin down. Further growth studies are required which tune the extension of the nano-facet

and, thereby, enable a more solid definition of its exact orientation. Such enhancement of the nano-facet or even its suppression for more homogeneous composition is likely possible by adjusting Sb content and growth kinetic parameters (e.g. V/III ratio and temperature) in order to reduce or increase adatom surface diffusion mobility, respectively.

4. Summary

In summary, we systematically investigated the selective area VS MBE of periodic InAsSb NW arrays on SiO$_2$-templated (111) Si substrates with respect to growth conditions and mask geometry. We find that the Sb-surfactant mediated suppression of the NW aspect ratio upon increasing Sb supply can be mitigated by decreasing the mask opening diameter, whereas the pitch is found to have a considerable influence on the Sb incorporation behavior. We further find a strong influence of the V/III ratio and the growth temperature on the morphology and Sb-content of our NWs where optimized growth conditions with V/III $\sim$ 14 and $T \sim$ 520 °C yield relatively high Sb-content, high aspect ratio NWs. Correlated structural and compositional investigations evidenced the formation of an unintentional core–shell structure with a Sb-depleted radial boundary layer together with Sb-depleted corner stripes which propagate outwards as growth proceeds from the SiO$_2$ mask opening towards the final NW growth tip. The complex compositional structure is found to be the result of nanoscale facets at the interfaces of the dominant crystal facets composing the NW. Analysis of the truncation angles of the nano-facets provides further possible candidate low-index facets responsible for the decomposition of the InAsSb NWs into the unintentional core–shell structure.

Acknowledgments

ORCID iDs

Daniel Ruhstorfer ● https://orcid.org/0000-0003-3268-7698
Gregor Koblmüller ● https://orcid.org/0000-0002-7228-0158

References

[1] Winkler G W, Wu Q S, Troyer M, Krogstrup P and Soluyanov A A 2016 *Phys. Rev. Lett.* **117** 076403
[2] Sestoft J E *et al* 2018 *Phys. Rev. Mater.* **2** 044202
[3] Frolov S M, Plissard S R, Nadj-Perge S, Kouwenhoven L P and Bakkers E P A M 2013 *MRS Bull.* **38** 809
[4] Tian Y, Sakr M R, Kinder J M, Liang D, MacDonald M J, Qiu R L J, Gao H-J and Gao X P A 2012 *Nano Lett.* **12** 6492
[5] van Weperen I, Plissard S R, Bakkers E P A M, Frolov S M and Kouwenhoven L P 2013 *Nano Lett.* **13** 378
[6] Mingo N 2004 *Appl. Phys. Lett.* **84** 2652
[7] Polman A and Atwater H A 2012 *Nat. Mater.* **11** 174
[8] Farrell A C, Lee W-J, Senanayake P, Haddad M A, Prikhodko S V and Huffaker D L 2015 *Nano Lett.* **15** 6614
[9] Svensson J, Anttu N, Vainorius N, Borg B M and Wernersson L-E 2013 *Nano Lett.* **13** 1380
[10] Thompson M D, Alhodaib A, Craig A P, Robson A, Aziz A, Krier A, Svensson J, Wernersson L-E, Sanchez A M and Marshall A R J 2016 *Nano Lett.* **16** 182
[11] Ren D, Azizur-Rahman K M, Rong Z, Juang B-C, Somasundaram S, Shahili M, Farrell A C, Williams B S and Huffaker D L 2019 *Nano Lett.* **19** 2793
[12] Alhodaib A, Noori Y J, Carrington P J, Sanchez A M, Thompson M D, Young R J, Krier A and Marshall A R J 2018 *Nano Lett.* **18** 235
[13] Borg B M, Dick K A, Eymery J and Wernersson L-E 2011 *Appl. Phys. Lett.* **98** 113104
[14] Du W-N, Yang X-G, Wang X-Y, Pan H-Y, Ji H-M, Luo S, Yang T and Wang Z-G 2014 *J. Cryst. Growth* **396** 33
[15] Ji X, Yang X, Du W, Pan H and Yang T 2016 *Nano Lett.* **16** 7580
[16] Sourribes M J L, Isakov I, Panfilova M, Liu H and Warburton P A 2014 *Nano Lett.* **14** 1643
[17] Potts H, Friedl M, Amaduzzi F, Tang K, Tütüncüoglu G, Matteini F, Llado E A, McIntyre P C and Fontcuberta i Morral A 2016 *Nano Lett.* **16** 637
[18] Zhuang Q D, Anyebe E A, Chen R, Liu H, Sanchez A M, Rajpalke M K, Veal T D, Wang Z M, Huang Y Z and Sun H D 2015 *Nano Lett.* **15** 1109
[19] Anyebe E A, Rajpalke M K, Veal T D, Jin C J, Wang Z M and Zhuang Q 2015 *Nano Res.* **8** 1309
[20] Ercolani D, Gemmi M, Nasi L, Rossi F, Pea M, Li A, Salviati G, Beltram F and Sorba L 2012 *Nanotechnology* **23** 115606
[21] Christensen N E, Satpathy S and Pawlowska Z 1987 *Phys. Rev. B* **36** 1032
[22] Dubrovskii V G, Sibirev N V, Harmand J C and Glas F 2008 *Phys. Rev. B* **78** 235301
[23] Borg B M and Wernersson L E 2013 *Nanotechnology* **24** 202001
[24] Kawaguchi K, Ekawa M, Akiyama T, Kuwatsuka H and Sugawara M 2006 *J. Cryst. Growth* **291** 154
[25] Zhuang Q D *et al* 2017 *Nanotechnology* **28** 105710
[26] Hertenberger S *et al* 2012 *Appl. Phys. Lett.* **101** 043116
[27] Koblmüller G and Abstreiter G 2014 *Phys. Status Solidi—RRL* **8** 11
[28] Robson M, Azizur-Rahman K M, Parent D, Wojdylo P, Thompson D A and LaPierre R R 2017 *Nano Futures* **1** 035001
[29] Sokolovskii A S, Robson M T, LaPierre R R and Dubrovskii V G 2019 *Nanotechnology* **30** 285601
[30] Li T, Gao L, Lei W, Guo L, Pan H, Yang T, Chen Y and Wang Z 2013 *Nanoscale Res. Lett.* **8** 333
[31] Hertenberger S, Rudolph D, Bichler M, Finley J J, Abstreiter G and Koblmüller G 2010 *J. Appl. Phys.* **108** 114316
[32] Ruhstorfer D, Mejia S, Ramsteiner M, Döblinger M, Riedl H, Finley J J and Koblmüller G 2020 *Appl. Phys. Lett.* **116** 052101
[33] Osakabe N, Tanishiro Y, Yagi K and Honjo G 1981 *Surf. Sci.* **109** 353
[34] Hertenberger S, Rudolph D, Bolte S, Döblinger M, Bichler M, Spirkoska D, Finley J J, Abstreiter G and Koblmüller G 2011 *Appl. Phys. Lett.* **98** 123114

[35] Yuan X, Caroff P, Wang F, Guo Y, Wang Y, Jackson H E, Smith L, Tan H H and Jagadish C 2015 *Adv. Funct. Mater.* **25** 5300

[36] Ahmad E, Karim M R, Hafiz S B, Reynolds C L, Liu Y and Iyer S 2017 *Sci. Rep.* **7** 10111

[37] Sonner M, Treu J, Saller K, Riedl H, Finley J J and Koblmüller G 2018 *Appl. Phys. Lett.* **112** 091904

[38] Treu J, Xu X, Ott K, Saller K, Abstreiter G, Finley J J and Koblmüller G 2019 *Nanotechnology* **30** 495703

[39] Björk M T, Schmid H, Breslin C M, Gignac L and Riel H 2012 *J. Cryst. Growth* **344** 31

[40] Kriegner D *et al* 2011 *Nano Lett.* **11** 1483

[41] Treu J, Speckbacher M, Saller K, Morkötter S, Döblinger M, Xu X, Riedl H, Abstreiter G, Finley J J and Koblmüller G 2016 *Appl. Phys. Lett.* **108** 053110

[42] del Giudice F, Becker J, de Rose C, Döblinger M, Ruhstorfer D, Suomenniemi L, Treu J, Riedl H, Finley J J and Koblmüller G 2020 *Nanoscale* **12** 21857–68

[43] Ikejiri K, Sato T, Yoshida H, Hiruma K, Motohisa J, Hara S and Fukui T 2008 *Nanotechnology* **19** 265604

[44] Dubrovskii V G, Cirlin G E, Soshnikov I P, Tonkikh A A, Sibirev N V, Samsonenko Y B and Ustinov V M 2005 *Phys. Rev.* B **71** 205325

[45] Koblmüller G, Hertenberger S, Vizbaras K, Bichler M, Bao F, Zhang J P and Abstreiter G 2010 *Nanotechnology* **21** 365602

[46] Borgstroem M T, Immink G, Ketelaars B, Algra R and Bakkers E P A M 2007 *Nat. Nanotechnol.* **2** 541

[47] Gotschke T, Schumann T, Limbach F, Stoica T and Calarco R 2011 *Appl. Phys. Lett.* **98** 103102

[48] Rudolph D, Schweickert L, Morkötter S, Loitsch B, Hertenberger S, Becker J, Bichler M, Abstreiter G, Finley J J and Koblmüller G 2014 *Appl. Phys. Lett.* **105** 033111

[49] Lugani L, Ercolani D, Beltram F and Sorba L 2011 *J. Cryst. Growth* **323** 304

[50] Ren D *et al* 2016 *Nano Lett.* **16** 1201

[51] Hertenberger S, Rudolph D, Becker J, Bichler M, Finley J J, Abstreiter G and Koblmüller G 2012 *Nanotechnology* **23** 235602

[52] Lee G S, Lo Y, Lin F, Bedair S M and Laidig W D 1985 *Appl. Phys. Lett.* **47** 1219

[53] Sarney W L, Svensson S P, Anderson E M, Lundquist A M, Pearson C and Millunchick J M 2014 *J. Cryst. Growth* **406** 8

[54] Dimroth F, Agert C and Bett A W 2003 *J. Cryst. Growth* **248** 265

[55] Sarney W L and Svensson S P 2015 *J. Vac. Sci. Technol.* B **33** 060604

[56] Morkötter S *et al* 2013 *Phys. Rev.* B **87** 205303

[57] Koblmüller G, Vizbaras K, Bolte S, Rudolph D, Becker J, Döblnger M, Amann M-C, Finley J J and Abstreiter G 2012 *Appl. Phys. Lett.* **101** 053103

[58] de la Mata M *et al* 2012 *Nano Lett.* **12** 2579

[59] Lim S K, Tambe M J, Brewster M M and Gradecak S 2008 *Nano Lett.* **8** 1386

[60] Xu T, Dick K A, Plissard S, Nguyen T H, Makoudi Y, Berthe M, Nys J-P, Wallart X, Grandidier B and Caroff P 2012 *Nanotechnology* **23** 095702

[61] Guo Y N *et al* 2013 *Nano Lett.* **13** 643

[62] Conesa-Boj S, Kriegner D, Han X-L, Plissard S, Wallart X, Stangl J, Fontcuberta i Morral A and Caroff P 2014 *Nano Lett.* **14** 326

[63] de Lepinau R, Scaccabarozzi A, Patriarche G, Travers L, Collin S, Cattoni A and Oehler F 2019 *Nanotechnology* **30** 294003

[64] Stettner T *et al* 2018 *Nano Lett.* **18** 6292

[65] Wagner J B, Sköld N, Wallenberg L R and Samuelson L 2010 *J. Cryst. Growth* **312** 1755

[66] Yuan X, Caroff P, Wong-Leung J, Tan H H and Jagadish C 2015 *Nanoscale* **7** 4995

[67] Ramdani M R, Harmand J C, Glas F, Patriarche G and Travers L 2012 *Cryst. Growth Des.* **13** 91

[68] Plissard S R, Slapak D R, Verheijen M A, Hocevar M, Immink G W G, van Weperen I, Nadj-Perge S, Frolov S M, Kouwenhoven L P and Bakkers E P A M 2012 *Nano Lett.* **12** 1794

[69] Rudolph D *et al* 2013 *Nano Lett.* **13** 1522

[70] Jeon N, Ruhstorfer D, Döblinger M, Matich S, Loitsch B, Koblmüller G and Lauhon L J 2018 *Nano Lett.* **18** 5179

[71] Chen C, Shehata S, Fradin C, LaPierre R, Couteau C and Weihs G 2007 *Nano Lett.* **7** 2584